ADVANCED FUNCTIONAL MATERIALS
www.afm-journal.de

Transforming an Ionic Conductor into an Electronic Conductor via Crystallization: In Situ Evolution of Transference Numbers and Structure in (La,Sr)(Ga,Fe)O_{3-x} Perovskite Thin Films

*Haley B. Buckner, Joshua Simpson-Gomez, Alexander Bonkowski, Kathrin Rübartsch, Hua Zhou, Roger A. De Souza, and Nicola H. Perry**

Mixed-conducting perovskites are workhorse electrochemically active materials, but typical high-temperature processing compromises their catalytic activity and chemo-mechanical integrity. Low-temperature pulsed laser deposition of amorphous films plus mild thermal annealing is an emerging route to form homogeneous mixed conductors with exceptional catalytic activity, but little is known about the evolution of the oxide-ion transport and transference numbers during crystallization. Here the coupled evolution of ionic and electronic transport behavior and structure in room-temperature-grown amorphous (La,Sr)(Ga,Fe)O_{3-x} films as they crystallize is explored. In situ ac-impedance spectroscopy with and without blocking electrodes, simultaneous capturingsynchrotron-grazing-incidence X-ray diffraction, dc polarization, transmission electron microscopy, and molecular dynamics simulations are combined to evaluate isothermal and non-isothermal crystallization effects and the role of grain boundaries on transference numbers. Ionic conductivity increases by ≈2 orders of magnitude during crystallization, with even larger increases in electronic conductivity. Consequently, as crystallinity increases, LSGF transitions from a predominantly ionic conductor to a predominantly electronic conductor. The roles of evolving lattice structural order, microstructure, and defect chemistry are examined. Grain boundaries appear relatively nonblocking electronically but significantly blocking ionically. The results demonstrate that ionic transference numbers can be tailored over a wide range by tuning crystallinity and microstructure without having to change the cation composition.

1. Introduction

Perovskite oxide mixed ionic and electronic conductors (MIECs) play an essential role as electrochemically active components of solid-state ionic devices (e.g., gas sensors, gas separation membranes, and electrodes for fuel/electrolysis cells). For these applications, surface oxygen exchange kinetics, ionic/electronic charge transport, and chemo-mechanical stability are the key factors governing performance.[1,2] Generally, operating at high temperatures (≈700–1000 °C)[3] yields sufficiently high electronic and ionic conductivities and rapid surface exchange kinetics for efficient device operation. Similarly, high-temperature fabrication processes (e.g., 600–800 °C for pulsed laser deposition of oxide thin films or 1200–1800 °C for bulk ceramics[4–7]) facilitate thermally activated diffusion and mixing of cations for homogeneous and well-crystallized perovskite structures. However, fabricating and operating at high temperatures leads to coarsening, segregation of impurities, dopants, and/or large A-site cations, and/or formation of passivating surface phases. These changes can reduce the catalytically

H. B. Buckner, J. Simpson-Gomez, N. H. Perry
Department of Materials Science & Engineering
University of Illinois at Urbana-Champaign
1304 W. Green St., Urbana, IL 61801, USA
E-mail: nhperry@illinois.edu

The ORCID identification number(s) for the author(s) of this article can be found under https://doi.org/10.1002/adfm.202401854

DOI: 10.1002/adfm.202401854

H. B. Buckner, N. H. Perry
Materials Research Laboratory
University of Illinois at Urbana-Champaign
104 S. Goodwin Ave., Urbana, IL 61801, USA

A. Bonkowski, K. Rübartsch, R. A. De Souza
Institute of Physical Chemistry
RWTH Aachen University
Landoltweg 2, 52056 Aachen, Germany

H. Zhou
Advanced Photon Source
Argonne National Laboratory
9700 S. Cass Avenue, Lemont, IL 60439, USA

active surface area, modify the surface electronic structure, and give rise to non-uniform surface chemistry[8,9] – all of which dramatically compromise the catalytic activity. An additional challenge with high-temperature fabrication and operation is the lattice contraction or expansion arising from oxygen stoichiometry changes and their electronic compensation. Stoichiometry gradients/changes in constrained device components can lead to excessive chemical stress,[10–12] eventually resulting in mechanical failure through cracking or delamination.[13] Taken together, the deleterious effects of high-temperature processing and usage motivate consideration of the low-temperature regime.

One promising route being explored is low-temperature pulsed laser deposition (PLD). For mixed conducting $La_{1-x}Sr_xO_{3-d}$ (LSC),[14–16] $SrTi_{1-x}Fe_xO_{3-d}$ (STF),[17,18] $Sr_2Ti_{1-x}Fe_xO_{4-d}$ (RP-STF),[19] and $SrTi_{1-x}Co_xO_{3-d}$ (STC)[19] films grown via PLD, decreasing the deposition temperature lowers the degree of crystallinity, with fully amorphous films typically formed below ≈450 °C.[14–16,18,19] Beneficial properties then emerge upon crystallization during an intermediate temperature anneal. In an in situ crystallization study of $SrTi_{0.65}Fe_{0.35}O_{3-d}$ (STF35),[17] amorphous-grown films were shown to oxidize with the onset of crystallization and undergo changes in cation coordination environment and microstructure. This chemo-mechanical evolution increased both hole concentration and mobility, resulting in the emergence of high electronic conductivity. The resulting facile electronic charge transfer is thought to support the rapid oxygen surface exchange kinetics observed in these just-crystallized MIEC films. Additionally, enhanced oxygen surface exchange kinetics in low-temperature-grown MIEC films have been linked to pristine surface chemistry, where the typical surface passivation via A-site cation segregation (e.g., in STF35 and STC35) is absent due to the low-temperature processing route.[17–19] These early studies focused on materials with predominant electronic conductivity in the crystalline state (high electronic transference numbers). By contrast, implications of the amorphous-to-crystalline transition for oxide-ion transport and transference number remain to be explored. In perovskite oxides, oxygen vacancy migration has been shown to proceed through a hopping mechanism, where oxide ions jump to the next site via a curved path along the BO_6 octahedral edge.[20] It follows that the amorphous-to-crystalline transition, and associated changes in bond length distributions, may have a significant impact on oxide-ion transport.[20] Considering the broader importance of low-temperature manufacturing routes when the thermal budget may be limited, and the benefit of low-temperature processing to MIEC performance to date, it is important to understand how crystallization impacts both the ionic and electronic transport and therefore to study the evolution of materials with different transference numbers.

To further the understanding of the impact of in situ crystallization on both ionic and electronic conductivity, we selected a new composition with an intermediate transference number. Lanthanum gallate-based perovskites are of interest for electrochemical devices, given their ability to exhibit exceptionally high oxide-ion conductivities.[21–31] High mixed ionic/electronic conductivities and a range of transference numbers can be achieved by, e.g., partial substitution of Sr on the A-site, or Mg or nominally multivalent transition metal cations on the B-site, to introduce oxygen vacancies and/or holes and support charge transport. In a series of studies, Kharton et al.[29,31,32] investigated the effect of B-site dopants on the charge transport behavior of $(La,Sr)(Ga,Mg,M)O_{3-x}$ (M = Ti,Cr,Fe,Co,Ni) compositions. They found that heavily substituting the Ga-site with Cr, Fe, Co, or Ni increases the electronic conductivity in the order of Cr < Fe < Co < Ni. The increase in electronic conductivity when increasing the transition metal dopant concentration above a "percolation limit" (≈30%–35%)[29] reflects a transition from a p-type polaron hopping mechanism to metallic behavior.[29] As a result, a wide range of composition-dependent ionic transference numbers (from 10^{-6} to 1) are observed. Compared with Fe-substituted $(La,Sr)GaO_{3-x}$, Co- and Ni- substitution resulted in the highest total conductivity and highest oxygen permeation rate, respectively.[28] In addition to compositional effects, the microstructure, particularly via grain boundary effects, also plays a large role in oxygen transport.[33–36] Altogether, $(La,Sr)(Ga,Fe)O_{3-x}$ (LSGF) has been identified as a composition of interest due to its intermediate transference number, giving ready experimental access to quantify both ionic and electronic conductivity. Given the scientific relevance of LSGF, the objective of this work is to evaluate the evolving ionic transference number and conductivity of in situ crystallized LSGF thin films.

Employing in situ synchrotron grazing incidence X-ray diffraction (GIXRD) with simultaneous ac impedance spectroscopy measurements, we directly correlate the developing crystal structure to the total and ionic conductivity. The amorphous films crystallize directly into an orthorhombic perovskite structure without secondary phase formation. Comparison of temperature-dependent AC-IS during crystallization with and without electronically blocking electrodes demonstrates that while ionic conductivity increases by ≈2 orders of magnitude during crystallization, the electronic conductivity increases by even more for an increase in total conductivity of over 4 orders of magnitude. As a result, the material transitions from being a predominantly ionic conductor to a predominantly electronic conductor as crystallinity increases. Additional ex situ DC polarization measurements of ionic transference numbers as a function of crystallinity confirm the AC-IS findings. One consequence of crystallization is the formation of a high density of grain boundaries as observed by transmission electron microscopy, coinciding with a strongly increased experimental activation energy for ionic conductivity, suggesting their blocking nature; therefore, the grain boundary effect on ionic transport is examined computationally. With increasing grain-boundary density, molecular dynamics (MD) simulations of crystalline LSGF confirm a decrease in oxygen transport rate and an increase in activation enthalpy. Taken together, the GIXRD, electrical measurements, microscopy (S/TEM-EDS) analyses, and MD simulations reveal that the oxygen transport behavior is significantly impacted by the microstructure, with blocking grain boundaries dominating the observed ionic conductivity after crystallization. By tuning the crystallinity and microstructure of the LSGF films, one can tailor ionic transference numbers to access ionic-dominant, mixed, and electronic-dominant conducting regimes. These results indicate enormous flexibility in the transport behavior without altering cation composition and further suggest promise for the use of semi-crystalline mixed conductors across a broad range of low-to-intermediate temperature applications.

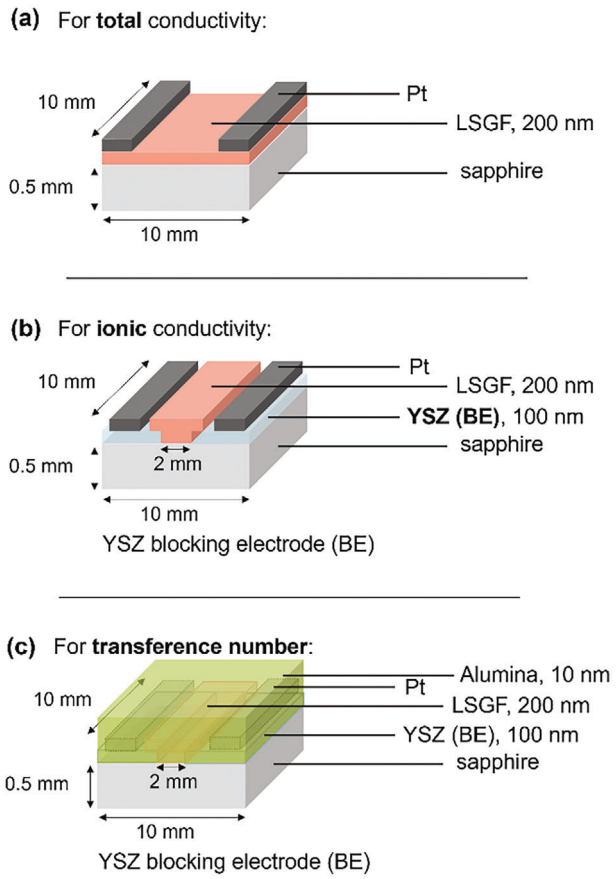

Figure 1. Schematic of sample geometries used to measure a) total conductivity, b) ionic conductivity using a YSZ blocking electrode, and c) transference numbers using a YSZ blocking electrode and an alumina capping layer (green). The diagrams are not drawn to scale.

2. Experimental Section

2.1. Sample Fabrication

For AC-IS and DC polarization measurements, 3 different sample geometries were employed to measure the 1) in-plane total conductivity, 2) in-plane ionic conductivity, and 3) ionic transference number, shown in **Figure 1**. To measure the total conductivity, amorphous LSGF was deposited directly onto a (0001)-oriented single crystalline Al_2O_3 substrates (MTI Corp., Richmond, CA USA) via room-temperature PLD, as seen in Figure 1a. To isolate the ionic conductivity from the total conductivity, crystalline YSZ was used as an electronically blocking electrode. As shown in Figure 1b, 2 strips of YSZ were deposited via PLD onto a (0001)-oriented single crystalline Al_2O_3 substrate (MTI Corp., Richmond, CA USA) at high temperature with a 2 mm wide strip masked with high-temperature polyimide tape (Protective Pak, Chino, CA). The film was cooled back to room temperature before amorphous LSGF was deposited at room temperature overlapping the 2 strips of YSZ. Then after PLD, 2 strip platinum current collectors were deposited on the surface of the film, with a 4 mm wide strip masked with high-temperature polyimide tape (Protective Pak, Chino, CA). Platinum wires were connected to the current collectors using silver paste (SPI Supplies, West Chester, PA). For the layered samples with a blocking electrode, the Pt current collectors were placed so that they only overlapped with the YSZ layer, not the LSGF layer. To determine the ionic transference numbers, again a YSZ blocking layer was used in the geometry described by Figure 1. Here, an additional Al_2O_3 capping layer was deposited by ALD over the entire sample to prevent oxygen exchange between the gas phase and the LSGF film during the DC polarization measurements. Pt wires were connected to the Pt strip electrodes with silver paste and wrapped in high-temperature polyimide tape prior to deposition of the alumina capping layer.

A $La_{0.7}Sr_{0.3}Ga_{0.6}Fe_{0.4}O_{3-x}$ (LSGF) target was prepared for pulsed laser deposition via solid state synthesis; powders of dried La_2O_3 (99.99+% purity, purchased from Fisher Scientific Company LLC, USA), $SrCO_3$ (99.99% purity, purchased from Fisher Scientific Company LLC, USA), Ga_2O_3 (99.99+% purity, purchased from Fisher Scientific Company LLC, USA), and Fe_2O_3 (99.995% purity, purchased from Fisher Scientific Company LLC, USA) powders were ground together in stoichiometric ratios, uniaxially pressed at 120 MPa, and calcined in air at 800 °C for 5 h using a heating and cooling rate of 2 °C min^{-1}. The calcined pellet was ground milled in ethanol for 1 h at room temperature and dried at 80 °C for 12 h. The dried, calcined powder was then uniaxially pressed at 120 MPa and sintered in air at 1450 °C for 8 h with heating and cooling at 2 °C min^{-1}. While not a single phase, the sintered LSGF target was found to agree with the desired cation ratio (La:Sr:Ga:Fe) for the desired perovskite phase, by X-ray fluorescence measurements (EDX-7000, Shimadzu, USA). For the 8YSZ target, 8YSZ powder (99.95% purity, purchased from Fisher Scientific Company LLC, USA) was uniaxially pressed into a pellet at 120 MPa and sintered at 1550 °C for 6 h using a heating/cooling rate of 2 °C min^{-1}. The sintered 8YSZ target was found to have the desired composition and structure, confirmed via X-ray diffraction (Bruker Advanced D8, Bruker Corp., USA)) in Bragg-Brentano geometry with Cu-K_α radiation.

PLD depositions for $La_{0.7}Sr_{0.3}Ga_{0.6}Fe_{0.4}O_{3-x}$ (LSGF, 200 nm thick) and 8mol% Y_2O_3-stabilized ZrO_2 (8YSZ, 100 nm thick) were carried out using a 248 nm KrF excimer laser (Lambda Physik, LPX 210) in a vacuum chamber (PVD Products, nano-PLD) evacuated to a base pressure of 3×10^{-6} Torr. During deposition, oxygen (AirGas, UHPOX 300) flowed into the chamber at 20 sccm to achieve a process pressure of 35 mTorr. The power of the laser, measured by an intelligent window upon entering the chamber, ranged from 0.07 to 0.10 W at a pulse frequency of 5 Hz. (The incident laser energy, prior to optics and windows, was set at ≈350 mJ.) LSGF films were deposited amorphous at room temperature (≈22 °C), and YSZ films were grown at 700 °C to achieve high crystalline quality. The growth rates for LSGF and YSZ were calibrated separately using X-ray reflectivity. While the LSGF films were each grown separately, the depositions were performed under the same conditions and close together in time to ensure consistent initial amorphous structures.

Platinum current collectors were deposited by DC magnetron sputtering (ATC Orion 8, AJA International, Inc., USA) at a DC power of 50 W under 3 mTorr of Ar, at room temperature. Alumina films (15 nm thick) were deposited by ALD at 80 °C using

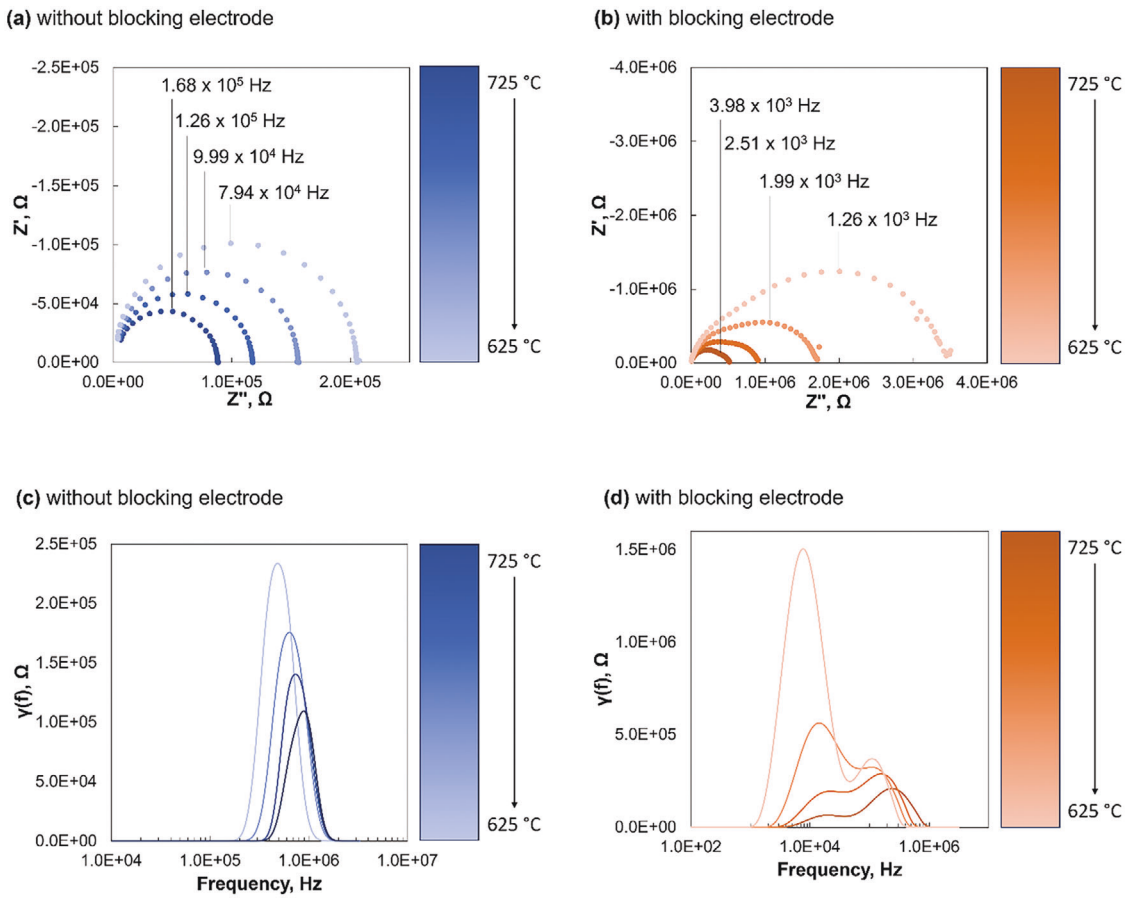

Figure 2. Sample impedance spectra as a function of temperature when measuring a) total conductivity and b) ionic conductivity of the LSGF film during cooling (after crystallization) and corresponding DRT spectra for samples c) without a YSZ blocking electrode and d) with a YSZ blocking electrode.

alternating 15 ms pulses of Trimethylaluminum (TMA) and H_2O with a 30 s delay between pulses.

2.2. In Situ Characterization During Crystallization (Structural Evolution)

A series of measurements were performed during in situ crystallization:

1) Temperature-dependent AC-IS of total conductivity.
2) Temperature-dependent AC-IS of ionic conductivity.
3) Isothermal AC-IS of total conductivity measurements in the lab.
4) Isothermal AC-IS of ionic conductivity measurements in the lab.
5) GIXRD with simultaneous AC-IS of isothermal total conductivity measurements at APS beamline 12-ID-D.
6) GIXRD with simultaneous AC-IS of isothermal ionic conductivity measurements at APS beamline 12-ID-D.

In situ, temperature-dependent impedance spectra were collected on separate samples during *nonisothermal* crystallization with and without blocking electrodes. Temperature-dependent measurements performed in the lab were conducted in a tube furnace (ThermoFisher Scientific, USA) with UHP O_2 and Ar gas flow controlled by rotameters with a ratio of 20 sccm O_2 to 80 sccm Ar. Since ac measurements were performed, the wires connecting the impedance analyzer to the sample were shielded by surrounding alumina tubes coated in platinum paint, and the temperature was monitored with a thermocouple positioned adjacent to the sample – separated by ≈2 mm. (Although full thermal equilibrium may not have been attained in non-isothermal measurements, the temperature at which the onset of crystallization was observed in this setup electrically matched that measured by DTA in a separate non-isothermal setup.) Using this experimental setup, the samples were heated from room temperature (≈22 °C) to 700 °C at a ramp rate of 5 °C min^{-1} and cooled back to room temperature at the same rate. Impedance spectra were collected every 30 s upon heating and cooling. Sample impedance spectra collected as a function of temperature when measuring total and ionic conductivity are shown in **Figure** 2a,b. To gain insight into the appropriate equivalent circuit, the impedance spectra from sample geometries with and without the blocking electrode were analyzed with a "distribution of relaxation times" (DRT) approach.[37–41] Only one peak is observed in the DRT spectra (Figure 2c) from total conductivity measurements without a blocking electrode; therefore, the

impedance spectra were fit with an R(RQ) equivalent circuit – a resistor, *R*, in series with a resistor and constant phase element, *Q*, in parallel. Because of noise from high resistances at lower temperatures on heating, values of resistance extracted from fitting impedance spectra were reported beginning at 520 °C. A YSZ blocking electrode was employed to measure the LSGF film's ionic conductivity, yielding 2 arcs in the impedance spectra (Figure 2b) and 2 corresponding peaks in the DRT spectra (Figure 2d). These impedance spectra were fit using a R(RQ)(RQ) equivalent circuit. Similarly, because of noise from high resistances at lower temperatures, resistances calculated from fitting the impedance spectra were reported starting at 560 °C on heating and down to 580 °C on cooling. Due to the large capacitance of the substrate, grain, and grain boundary features are not separable in most polycrystalline thin films.[42,43] Additionally, temperature-dependent resistances extracted from the high-frequency arc, shown in an Arrhenius plot in Figure S1 (Supporting Information), yield activation energy and magnitude of conductivity consistent with those of YSZ thin films reported in the literature.[44,45] Thus, the resistance associated with the high-frequency arc is attributed to the YSZ blocking electrode, and that of the low-frequency arc is attributed to the LSGF mixed conducting thin film. The conductivities were calculated using the resistance from the LSGF arc and sample geometry. From the temperature-dependent AC-IS measurements, ionic transference numbers were calculated for LSGF with increasing crystallinity on heating from the ratio of ionic conductivity to total conductivity.

In situ, isothermal AC-IS was also used to monitor conductivity (either total or ionic conductivity depending on sample cell type) of crystallizing LSGF thin films using a single zone tube furnace with a controlled gas atmosphere (≈0.2 atm O_2, 0.8 atm Ar) using high purity gases and a 100 sccm rotameter-controlled flow rate. The total conductivity and ionic conductivity were each measured separately during the crystallization of 2 amorphous-grown LSGF films. As previously described, a YSZ blocking electrode was employed to measure ionic conductivity. After room temperature LSGF deposition, the samples were heated to 700 °C, held isothermally for 3 h, and then slowly cooled to room temperature at 5 °C min^{-1}. AC-IS spectra were collected using a sinusoidal voltage amplitude of 0.3 V centered at 0 V in a frequency range from 1 MHz to 10 Hz. The in-plane conductivity was determined by fitting impedance spectra with an equivalent circuit. When calculating the total conductivity, the impedance spectra were fit in ZPlot (Scribner Associates Inc., USA) with an R(RQ) equivalent circuit, where Q is a constant phase element. When calculating the ionic conductivity, the impedance spectra were fit with an R(RQ)(RQ) equivalent circuit, where the high-frequency (RQ) circuit is representative of the YSZ blocking electrode and the low-frequency arc is from the LSGF film. The conductivity of the LSGF film was calculated using the extracted resistance and sample geometry.

Synchrotron GIXRD experiments were carried out at beamline 12-ID-D of the Advanced Photon Source at Argonne National Laboratory. A heating stage was applied to perform the in situ GIXRD experiments in air. Because electrical measurements were performed simultaneously at the beamline, the sample was positioned such that the X-ray beam was incident on the film surface between the strip Pt electrodes. Silver paste (SPI Supplies, USA) was applied to the back of the substrate to secure the sample to the stage, and the heating stage was heated to 100 °C for 1 h to cure the paste. The GIXRD data were collected at an incidence angle of 0.3° using an Eiger2 R K500 detector (pixel size: 75 × 75 μm^2, total area: 1030 × 514 pixels, Si sensor thickness: 450 µm) (Bruker, USA). The detector was exposed for 0.5 s per scan. Using a Si(111) double crystal monochromator, the X-ray energy was selected to be 20 keV, and the sample-to-detector distance (120 cm), detector tilt angle, and detector tilt rotation were calibrated in GSAS-II using a CeO_2 single crystal standard.

To monitor the evolving structure and charge transport behavior during crystallization, amorphous LSGF films were heated from 100 to 700 °C at a ramp rate of 18 °C min^{-1} and then held isothermally for 5 h to crystallize the film. 2D X-ray diffraction patterns were collected every 2 s during heating and during the first 3 h of the isothermal hold. The collection rate was decreased to 1 scan per 10 s for the remaining 2 h of the isothermal hold and the cool down to room temperature. Simultaneously with the GIXRD measurements, ac impedance spectra were collected every minute during the thermal cycle. This experiment was repeated using samples with and without YSZ blocking electrodes to measure the ionic and total conductivity during crystallization, respectively, while monitoring the evolving structure with GIXRD.

The collected 2D diffraction patterns were integrated into GSAS-II software using a 2θ range from 3° to 30° (X-ray energy E = 20 keV) with masks to exclude strong diffraction spots from the sapphire substrate and spot masks (with a 3σ deviation threshold for rejection) to exclude scattering from surrounding metal on the sample or sample stage. Using the integrated diffraction patterns, the peak positions, intensities, and widths were refined sequentially, and the unit cell structure was auto-indexed within the GSAS-II software. All Bravais lattices were searched as possible solutions, and an orthorhombic unit cell (*Imma*) achieved the best fit, indicated by the highest M20 factor and no unindexed peaks. Rietveld refinements were performed in GSAS-II, initiated from a previously determined structure file for $LaGaO_3$ (*Imma*, mp-556983) from Materials Project. The background was fit with a 5th-order Chebychev polynomial. Then, lattice parameters were refined first, followed sequentially by domain size, microstrain, atomic coordinates, and thermal parameters.

To examine any impact of time-varying impedance during the dynamic film evolution on the acquired impedance spectra, equivalent circuit fits and Kramers-Kronig transforms were examined in Nyquist and Bode plot format, along with distribution of relaxation times analyses; results are shown in Figures S2–S11 (Supporting Information) and discussed in the Supporting Information. The analysis was performed for both isothermal and non-isothermal measurements.

2.3. Ex Situ Characterization (Static Structure)

A series of measurements were performed before or after varying degrees of in situ crystallization:

1) DC polarization of as-deposited (amorphous) LSGF film.
2) DC polarization of LSGF film annealed for 20 min.

3) DC polarization of LSGF film annealed for 3 h.
4) S/TEM imaging of LSGF film annealed for 20 min.
5) S/TEM imaging of LSGF film annealed for 3 h.

Amorphous LSGF films (with the YSZ blocking electrode) were each annealed separately at 700 °C in a sealed tube furnace with rotameter-controlled gas atmosphere (20 sccm UHP O_2 and 80 sccm UHP Ar, (Airgas, USA)) for 20 min and 3 h to achieve varying degrees of crystallinity. After crystallizing the films to different extents, an alumina capping layer was deposited over the entire sample surface by ALD to prevent the film from exchanging oxygen with the gas phase during the DC polarization measurement. The 2-point DC measurements were carried out at 600 °C using a Solartron Analytical impedance analyzer. The impedance analyzer includes an attached potentiostat and femtoammeter for applying DC biases and measuring small currents for high-impedance samples, respectively. A constant DC bias of 0.5 V was applied with the potentiostat across the Pt current collectors on the surface of the sample – directly in contact with the YSZ blocking electrodes but not the LSGF film, and the current was measured using the femtoammeter as a function of time as it decayed to a steady state. The steady-state current is representative of only ionic charge carrier transport if the ionic conductance in LSGF is much higher than the electronic conductance in the blocking electrode – YSZ. Once this condition is met, the ionic transference number is calculated using the ratio of the steady state current I_{ss} to the initial current I_0.

Additionally, the resultant microstructure of crystallized LSGF films was imaged using scanning transmission electron microscopy (S/TEM). A gold film (≈10 nm) was deposited onto the surface of the annealed LSGF samples (as deposited, 20 min, 3 h) to prevent charging. Cross sections were prepared for S/TEM and EDS using a lift-out technique using a dual-beam focused ion beam/ scanning electron microscope (Scios 2 SEM/FIB, ThermoFisher Sci.) after depositing an additional 2.5 µm of Pt in the FIB as a surface protection layer during lift-out. The cross sections were prepared and sequentially thinned at lower voltages (30 kV, 5 kV, 2 kV) to reduce beam damage to the lamellae. The microstructure and composition were analyzed using a Talos F200X G2 S/TEM operated at 200 kV using a Ceta camera for bright field imaging and a high-angle annular dark field (HAADF) detector for dark field imaging. ImageJ was used to determine average pore sizes (area/perimeter) and circularity. The circularity is defined by:

$$c = \frac{4\pi A}{P} \tag{1}$$

where A is the area of the outlined feature, and P is the perimeter. Values of the circularity less than 1 indicate a deviation from a perfect circle from elongation.

2.4. Computational Methods

Molecular dynamics simulations were used to determine oxygen tracer diffusion coefficients in cubic LSGF simulation cells with varying grain boundary densities: 1 grain (monocrystalline), 2 grains, and 5 grains. MD simulations were carried out in the LAMMPS code.[46] A set of empirical pair potentials.[20,47,48] based on the Born model of ionic solids, (with a cut-off of 12 Å), was used as the force field. Simulations were performed in the *NpT* ensemble with periodic boundary conditions at various temperatures in the range of 1300 ≤ T [K] ≤ 2800 and a pressure of p = 1 atm.

Monocrystalline cells were created by a 20 × 20 × 20 expansion of the cubic $Pm\bar{3}m$ $LaFeO_3$ unit cell and thus contained 40 000 ions. The target composition was achieved by randomly replacing 30% of lanthanum ions with strontium ions and 60% of iron ions with gallium ions, respectively. Oxygen vacancies were introduced, i.e., oxide ions were removed, until the total cell charge was zero. Polycrystalline cells containing 2 or 5 grains were constructed with the ATOMSK code.[49] The cells were created by placing grains of $LaFeO_3$ in a cubic simulation cell with cell dimensions of 80 Å × 80 Å × 80 Å, and thus with ca. 40 000 ions. For ion pairs at the boundaries separated by less than 1.5 Å, one ion was removed at random. To avoid A:B≠1, cations at the grain boundary were removed until the numbers of A- and B-site ions were identical. Subsequently, strontium- and gallium-containing cells were obtained by replacing at random the appropriate fraction of lanthanum and iron ions, respectively. Oxide ions were removed at random to achieve a charge-neutral simulation cell. In order to be able to estimate the variability of the polycrystalline structures, 2 randomly generated cells were constructed for both the 2-grain and the 5-grain case, resulting in a total of 4 simulation cells. Constant composition was used for the entirety of each simulation (i.e., the degree of oxygen deficiency does not vary with temperature or crystallinity). The oxygen tracer diffusion coefficient was calculated from 1300 K to 2800 K for cubic LSGF and then extrapolated down to experimentally relevant temperatures. No cation defects were introduced into the cubic cell, so cation diffusion coefficients were not calculated.

3. Results

Amorphous films were heated to 700 °C and held at temperature for 5 h to crystallize the films. In situ, GIXRD scans with simultaneous impedance spectroscopy measurements were carried out during this isothermal crystallization of amorphous-grown LSGF thin films. **Figure** 3a–c shows 3 sample snapshots of the 2D XRD patterns collected over the isothermal hold directly after the film reaches 700 °C, after 20 min of annealing, and after 3 h of annealing at 700 °C. The diffraction rings from the crystallizing LSGF film are marked with white arrows. No impurity phases are evident. The bright diffraction spots between LSGF rings arise from scattering from the Pt wires or other metals on the sample stage. Initially, no film diffraction peaks from the LSGF film are present. After annealing for 20 min, multiple diffraction rings characteristic of a perovskite structure appeared, which gradually became more intense over 3 h.

To gain more detailed insight into the evolving crystal structure, all 2D diffraction patterns over the 5-h isothermal hold were integrated (Figure 3d, which shows integrated data collected in the first 336 s), and peak positions, intensities, and widths were refined with an orthorhombic perovskite structure using GSAS-II software. Unit cell lattice parameters (Figure 3e,f) of the LSGF film, using the integrated data, are plotted as a function of time at 700 °C, revealing an initial lattice expansion and subsequent contraction of the crystalline portion of the film. Time $t = 0$ is

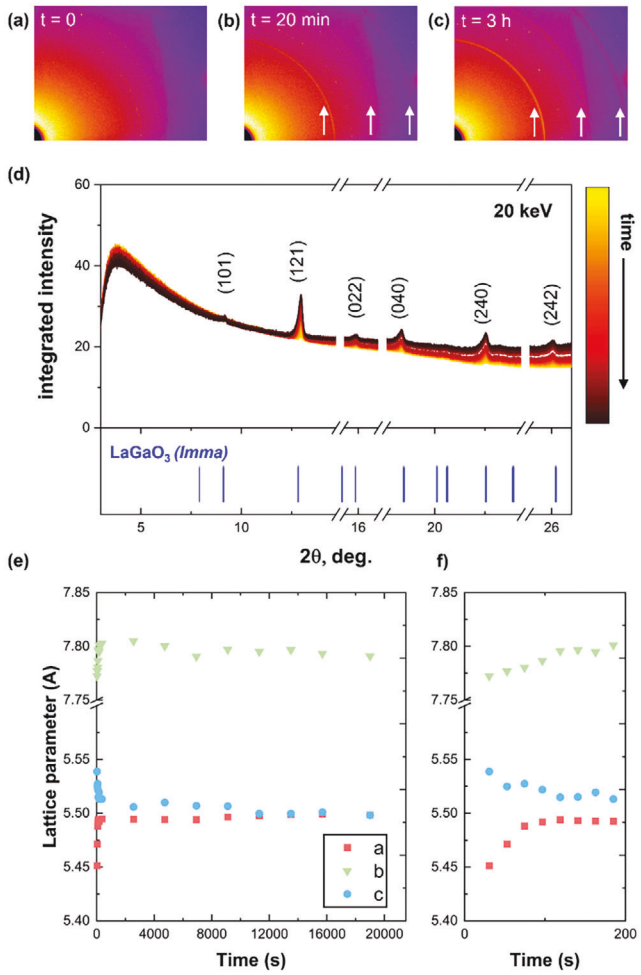

Figure 3. 2D diffraction patterns collected a) just as the sample reaches 700 °C, b) after 20 min at 700 °C b), and after 3 h at 700 °C c). The integrated 1D diffraction patterns d) are shown in a time series for t = 0–336 s. 1D peak positions for orthorhombic Imma $LaGaO_3$ (mp-556983) are shown in blue below the integrated 1D patterns for crystallizing LSGF. Line breaks (14.7°–15.3°, 17°–17.5°, and 24.3°–24.9°) are used to indicate the areas masked in the 2D patterns from extraneous scattering from the Pt current collectors/wires and metal heating stage. Lattice parameter evolution during 700 °C isothermal hold in air at beamline 12-ID-D over the full isothermal hold e) and over the first 200 s after the onset of crystallization f).

defined as the time at which the sample reaches 700 °C. **Table 1** shows the time evolution of orthorhombic (*Imma*) lattice parameters (a, b, and c), unit cell volume (V), and lattice parameter ratios in crystalline, diffracting regions during crystallization at 700 °C. Just after crystallization at $t = 30$ s (i.e., when diffraction peaks from LSGF become distinguishable above noise), the lattice parameters are $a = 5.451$ Å, $b = 7.772$ Å, and $c = 5.539$ Å. As crystallization proceeds, a and b lattice parameters increase while the c lattice parameter decreases with $a = 5.492$ Å, $b = 7.787$ Å, and $c = 5.522$ Å at $t = 97$ s. The b lattice parameter further increases to a maximum value $b = 7.805$ Å at $t = 2563$ s, and a and c continue to converge, with $a = 5.494$ Å and $c = 5.506$ Å at this point. At $t = 21\,993$ s (≈6 h), the a, b, and c lattice parameters reach final values of $a = 5.495$ Å, $b = 7.783$ Å, and $c = 5.497$ Å. Pseudocubic lattice

Table 1. Time evolution of orthorhombic (*Imma*) lattice parameters a, b, and c), unit cell volume (V), and lattice parameter ratios in crystalline, diffracting regions during crystallization at 700 °C. To reach a cubic structure, b/a ≈ 1.414, and c/a = 1.

Time, s	a, Å	b, Å	c, Å	b/a	c/a	V, Å^3
31	5.451	7.772	5.539	1.426	1.016	234.680
53	5.471	7.777	5.525	1.421	1.010	235.082
75	5.488	7.780	5.527	1.418	1.007	236.019
97	5.492	7.787	5.522	1.418	1.005	236.128
119	5.494	7.796	5.515	1.419	1.004	236.184
141	5.493	7.797	5.515	1.419	1.004	236.195
163	5.493	7.795	5.519	1.419	1.005	236.309
185	5.493	7.801	5.513	1.420	1.004	236.226
372	5.495	7.803	5.513	1.420	1.003	236.375
2563	5.494	7.805	5.506	1.421	1.002	236.110
4740	5.494	7.800	5.510	1.420	1.003	236.129
6939	5.494	7.791	5.507	1.418	1.002	235.706
9114	5.496	7.797	5.507	1.419	1.002	235.982
11 308	5.498	7.795	5.500	1.418	1.000	235.693
13 503	5.499	7.797	5.500	1.418	1.000	235.780
15 697	5.499	7.793	5.501	1.417	1.000	235.758
19 015	5.498	7.791	5.498	1.417	1.000	235.524
21 998	5.495	7.783	5.497	1.416	1.000	235.111

parameter ratios are $b_{pc}/a_{pc} = 1.0082$ and $c_{pc}/a_{pc} = 1.0161$ just after crystallization ($t = 30$ s), versus $b_{pc}/a_{pc} = 1.0015$ and $c_{pc}/a_{pc} = 1.0004$ after ≈6 h, indicating an evolution toward the more symmetric cubic structure as crystallization progresses. Through the entirety of the 700 °C isothermal anneal, a distinct, broad amorphous hump centered at 3.84° (2θ) is observed, but the intensity of the amorphous feature decreases over time, consistent with an increase in crystallinity of the film.

To view the change in the microstructure of the films, cross sections for LSGF thin films were studied by transmission electron microscopy (TEM) and scanning transmission electron microscopy (STEM). HAADF STEM images are shown for amorphous-grown LSGF films after annealing at 700 °C for 20 min (**Figures** 4a) and 3 h (Figure 4b). After annealing for 20 min at 700 °C, extensive porosity has formed, with an average pore area and perimeter of 93 nm^2 and 42 nm, respectively. With further annealing for 3 h, the average pore area and perimeter increase to 264 nm^2 and 85 nm, respectively. The pore connectivity has increased, as demonstrated by a decrease in average circularity from 0.62 at 20 min to 0.50 at 3 h. With the formation of pore chains with limited open porosity, the connected pores become more elongated and tortuous, resulting in a decrease in circularity. Bright-field TEM micrographs reveal the LSGF film annealed for 20 min is comprised of mostly small, round crystallites (≈5 nm diameter, N = 10) along with a couple of much larger crystallites (≈17 nm diameter, N = 2), giving an average crystallite area of 46 nm^2 (N = 12) and average circularity of 0.81. With further annealing, the average grain diameter increases to 14 nm (N = 11) and maintains an average circularity of 0.82. In both cases, the apparent average grain diameter is on the order of ≈10 nm, suggesting a high grain boundary density.

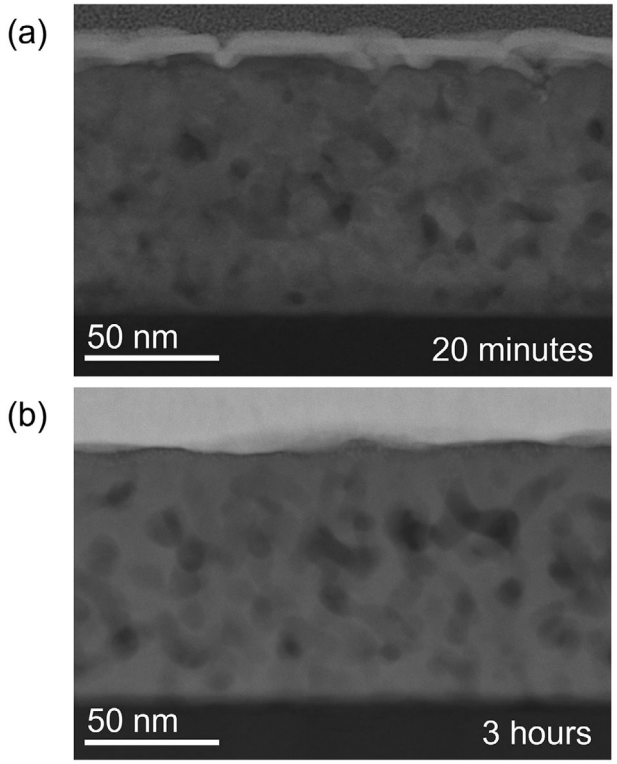

Figure 4. HAADF STEM micrographs of amorphous-grown LSGF thin films annealed for a) 20 min and b) 3 h at 700 °C.

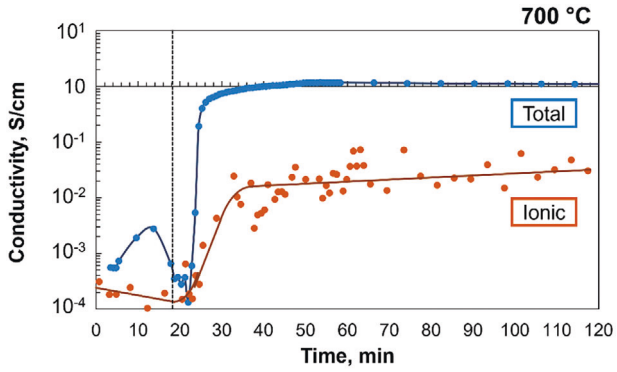

Figure 5. a) Total conductivity and b) ionic conductivity of an amorphous-grown LSGF3040 film during isothermal crystallization at APS beamline 12-ID-D. The sample reaches the 700 °C set point at t = 18 min, marked with a vertical dashed line. Solid lines are a guide to the eye.

To investigate how the total and ionic conductivities change during crystallization, in situ, AC-IS measurements were conducted simultaneously with the GIXRD measurements at the synchrotron experimental hutch. Data collected at the beamline were somewhat noisy due to unshielded wires and additional connectors needed for the experimental setup. **Figure 5** shows the change in total conductivity and ionic conductivity overtime at 700 °C. The total conductivity data were collected simultaneously with the GIXRD data shown in Figure 3. The ionic conductivity data were collected using the same experimental setup at APS beamline 12-ID-D but with a different sample with a YSZ

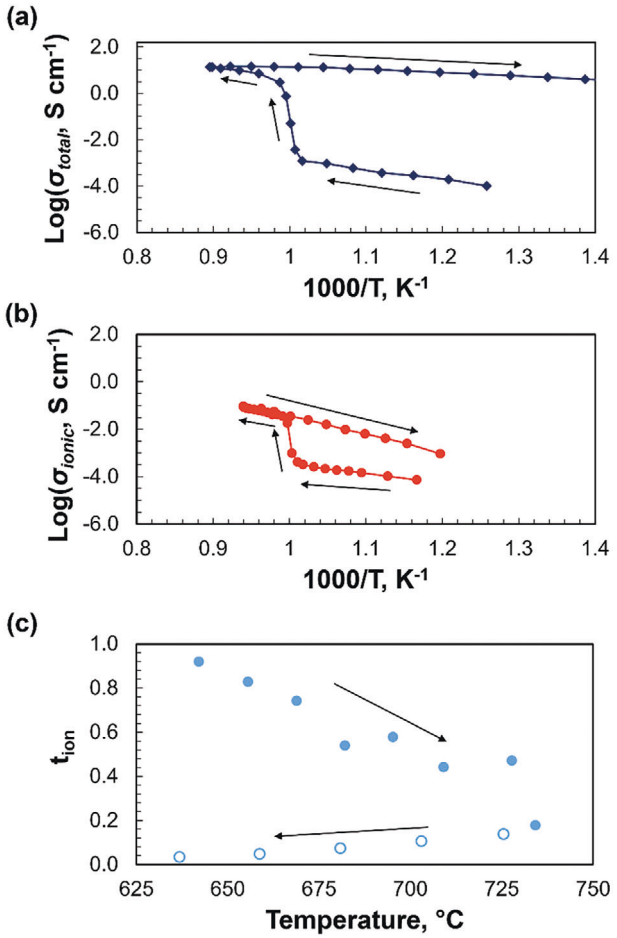

Figure 6. Change in a) total conductivity and b) ionic conductivity over a temperature ramp from 25 to 750 °C. c) ionic transference number calculated during crystallization on heating (solid) and on cooling (open) after crystallization. Arrows indicate heating/cooling directions.

blocking electrode. The times were synchronized via the time the 700 °C set point was reached (t = 18 min), marked with a vertical dashed line in Figure 5. Diffraction rings consistent with a perovskite phase appear shortly after the set point is reached. Before the appearance of the diffraction rings, an initial non-monotonic change in conductivity is observed. As the film crystallizes, the total conductivity increases over 4 orders of magnitude, increasing from 5.61×10^{-5} S cm^{-1} to 1.15 S cm^{-1} at 700 °C after 35 min of annealing. The ionic conductivity also increases but to a much lesser extent. Directly after the 700 °C set point is reached, the ionic conductivity is 1.50×10^{-3} S cm^{-1} and increases to 3.52×10^{-1} S cm^{-1} after 35 min.

In addition to these isothermal crystallization studies, the total and ionic conductivities were investigated experimentally as a function of temperature during crystallization, shown in the Arrhenius plot in **Figure 6**a. Activation energies for amorphous versus crystalline LSGF were determined assuming a hopping-type conductivity (for electronic and ionic), of the form:

$$\sigma = \left(\frac{B}{T}\right) e^{-E_A/k_B T} \quad (2)$$

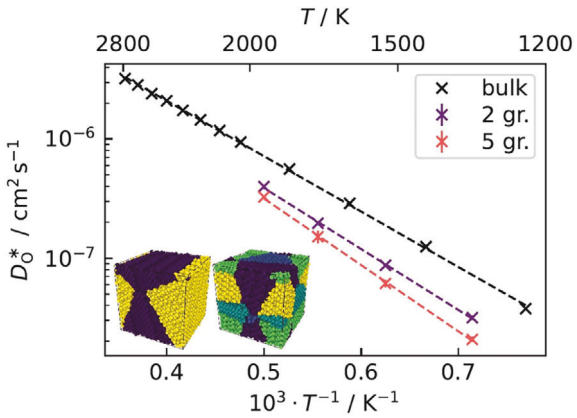

Figure 7. Arrhenius plot of oxygen tracer diffusivities from MD simulation using cells with 1 (bulk), 2, and 5 grains. Diffusivities decrease and activation enthalpies increase as more grain boundaries are introduced. Inset: Exemplary polycrystalline simulation cells with 2 (left) and 5 (right) grains, respectively. The colors indicate different grains.

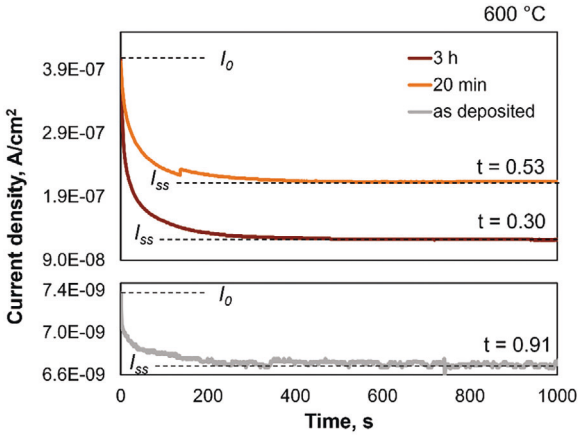

Figure 8. Current density over time with an in-plane DC bias for DC polarization measurements at 600 °C on an as-deposited LSGF film (grey) and films annealed for 20 min (orange) and 3 h (brown). Values of ionic transference number (inset) are calculated using the ratio of the steady state current I_{ss} to the initial current I_0.

where σ is the conductivity, B is the pre-exponential factor, E_A is the activation energy, k_B is Boltzmann's constant, and T is temperature. Upon heating, the total conductivity of the amorphous film initially increases linearly, yielding an activation energy of 0.86 ± 0.05 eV. Then, there is a dramatic increase in conductivity from 710 to 740 °C, indicative of crystallization. This behavior is irreversible. After crystallization and upon cooling, the slope decreases, giving an activation energy of 0.35 ± 0.05 eV for in situ crystallized LSGF. In stark contrast to the behavior of the total conductivity, the activation energy for ionic conductivity increases from 0.82 ± 0.05 eV for amorphous LSGF to 1.34 ± 0.05 eV after crystallization (Figure 6b). Ionic transference numbers were extracted from the temperature-dependent total and ionic conductivity measurements before and after crystallization (Figure 6c). On heating, the ionic transference number decreases significantly from 0.92 for fully amorphous LSGF to 0.18 after crystallization, indicating LSGF transitions from a predominantly ionic conductor to a predominantly electronic conductor with increasing crystallinity.

To computationally evaluate the impact of grain boundary density on oxide ion transport in crystalline LSGF, the oxygen tracer diffusivity was calculated with molecular dynamics simulations for cubic LSGF as a function of temperature for cells with 1, 2, and 5 crystalline grains, shown in **Figure 7**. The approximate grain volumes in these simulated structures are 500, 250, and 100 nm^3, respectively. Experimentally, the grain sizes are determined from 2D projections of the 3D structure via electron microscopy. For a more direct comparison with the experimental results, the grain area for each simulated structure was calculated to be 63, 40, and 22 nm^2, assuming spherical grains. Experimentally, in crystallized LSGF the average grain area increases from 46 nm^2 with 20 min of annealing (N = 11) to 175 nm^2 after 3 h (N = 10). As grain boundaries are introduced, the oxygen tracer diffusivity decreases. The activation enthalpy of oxygen diffusion increases monotonically with the number of grains in the simulation cell, starting at 0.92 ± 0.02 eV for monocrystalline (bulk) LSGF and increasing to 1.02 ± 0.02 eV with 2 grains and 1.11 ± 0.02 eV with 5 grains. As the crystallization of amorphous LSGF thin films introduces grain boundaries to the system, this result is consistent with the experimental findings showing an increase in activation energy for ionic conductivity after crystallization.

To confirm the effect of crystallinity on the ionic transference number, DC polarization measurements were carried out at 600 °C using a YSZ electronically-blocking electrode. The 3 separate films under investigation were a) as-deposited, b) annealed for 20 min at 700 °C, and c) annealed for 3 h at 700 °C. For all samples, the measured current decays to a steady state current when a DC voltage is applied across the Pt current collectors, as shown in **Figure 8**. The calculated ionic transference number at 600 °C for the as-deposited LSGF film was 0.91, indicating amorphous LSGF is a predominantly ionic conductor. After annealing, the measured currents increase by nearly 3 orders of magnitude, consistent with crystallization. The ionic transference number at 600 °C decreases to 0.53 and further to 0.30 when annealed for 20 min and 3 h at 700 °C, respectively.

4. Discussion

4.1. Structural Evolution of the Lattice

In situ, GIXRD measurements (Figure 3) show amorphous-grown LSGF thin films crystallize directly into an orthorhombic perovskite structure, with crystallinity increasing over time when held at 700 °C. This phase differs from observed crystal structures for high-temperature processed, polycrystalline solid solutions of $SrFeO_3$ and $LaGaO_3$ in literature. The crystal structure of $SrFeO_3$-$LaGaO_3$ solid solutions has been reported as rhombohedral $R\bar{3}c$ or cubic $Pm\bar{3}m$ at room temperature.[31,50,51] When Sr is not present on the A-site [i.e., $La(Ga,Fe)O_{3-x}$], an orthorhombic *Pnma* structure has been observed.[32] Using high-temperature X-ray and neutron diffraction, distorted perovskites [e.g., $La_{1-x}Sr_xGa_{1-y}Fe_yO_{3-d}$ (x = 0.2–0.8, y = 0–0.5)] at room temperature have been shown to undergo a phase transition to a highly ordered cubic $Pm\bar{3}m$ structure at elevated temperatures.[31,51] By

contrast, in situ crystallized LSGF studied here maintains an orthorhombic structure at 700 °C.[30] Analysis of the lattice parameters does suggest an approach toward the more symmetric cubic structure as crystallization proceeds though (ratios of pseudocubic lattice parameters approach 1 overtime at 700 °C; see Table 1). Given the complex evolution of lattice volume in the crystalline grains observed during this process (Table 1), the subtle structural change of the perovskite unit cell may arise from crystallization-induced strains as grains nucleate and grow within the amorphous matrix. These lattice strains are also expected to be accompanied by changes in the anion stoichiometry, given the association of crystallization and contraction with oxidation (discussed further below). Although the further possibility of local cation stoichiometry changes during crystallization has not been evaluated here, which could also contribute to the variable lattice distortions, we note that the in situ crystallization appears to avoid secondary phases or intermediate phase formation, which is very common with high-temperature processing of crystalline lanthanum gallate-based perovskites. Common segregated impurity phases found in materials with high Sr and Ga concentrations are $LaSrGaO_4$ and $SrLaGa_3O_7$.[31,52–54] The reasons for the apparent phase purity of the crystallizing films are not unambiguously known, but we hypothesize that the cations may be very well-mixed in the amorphous films with only small cation displacements needed to form the perovskite phase; the stress state may also differ from bulk materials, and avoidance of high-temperature processing may kinetically trap cations with a tendency to segregate.

4.2. Microstructural Evolution

BF TEM micrographs (Figure 4) indicate a high density of grain boundaries in the crystallized films, with grain diameters on the order of ≈8 nm after 20 min of annealing and ≈14 nm after 3 h of annealing. The development of grain boundaries has implications for the transport behavior comparison between amorphous and nanocrystalline films, discussed below. Additionally, nanoscale pores form during crystallization, and as crystallinity increases, pore connectivity increases. The pore evolution is likely related to strain development in the solid phase, which might arise from both oxidation and crystallization. As crystallization proceeds in LSGF films, there is an initial expansion and subsequent contraction of the unit cell volume (Figure 3e,f and Table 1) and a tendency toward the more symmetric cubic structure, suggesting a complex evolution of strain in crystallizing films that can explain the pore evolution. A similar expansion then contraction behavior has been reported in crystallizing STF35[17,55] and $BaTiO_3$ thin films,[55] though the source of the non-monotonic behavior has yet to be identified. For the case of STF35, both Fe K-edge position changes in X-ray absorption spectroscopy and optical absorption changes point to the role of oxidation during crystallization.[17] A similar change in color of the LSGF thin films, from mostly transparent, as-deposited, to a darker orange/brown color after annealing is observed. This optical evolution is likely consistent with oxidation occurring with the onset of crystallization, playing an important role in the structural and electrical evolution.

4.3. Ionic Conductivity Evolution

The ionic conductivity of amorphous-grown LSGF thin films increases by ≈2 orders of magnitude as a result of crystallization, reaching a value of 2.66×10^{-3} S cm^{-1} at 600 °C after crystallization (Figure 6b). Values of ionic conductivity for polycrystalline, bulk LSGF reported in literature vary from 0.97 S cm^{-1} to 4.14 S cm^{-1} at ≈0.2 atm O_2 and 600 °C, using several different experimental techniques.[27,29,31,56,57] (In some experiments, the ionic conductivity was calculated from oxygen permeation measurements under a chemical potential gradient, while others applied electrical methods, i.e., DC four-probe method or AC impedance spectroscopy.) The experimentally measured magnitude of ionic conductivity in bulk LSGF is ≈3 orders of magnitude larger than that of the crystallized LSGF films. This discrepancy may arise from the considerably higher grain boundary volume fraction in the thin films, with grain boundaries blocking ionic transport. Grain-boundary ionic conductivities 2–3 orders of magnitude below those of the grains are typical for oxide-ion conductors.[27,31,56,57] This interpretation is further supported in the present work by the increase in activation energy for ionic conductivity after crystallization, measured using temperature-dependent AC-IS measurements with electronically blocking electrodes (Figure 6b). A study on columnar-grained $La_{0.8}Sr_{0.2}Ga_{0.8}Mg_{0.2}O_{3-d}$ thin films demonstrated that the activation energy for ionic conductivity monotonically increased with increasing grain-boundary density.[58] A recent MD study[34] on polycrystalline $La_{0.6}Sr_{0.4}FeO_{3-x}$ demonstrated that at high temperatures grain boundaries impede oxygen transport, resulting in lower grain-boundary diffusivity compared to diffusivity in the grains. Similarly in the present work, the MD simulations demonstrate an increase in activation enthalpy of oxygen tracer diffusion with increasing grain-boundary density, providing further support for this interpretation. The experimentally determined activation energy for oxygen transport (1.34 eV) in the nanocrystalline LSGF film is just slightly higher than the MD-simulated oxygen migration enthalpy for polycrystalline LSGF (1.11 eV). One interpretation of this small discrepancy is that it arises from differences in grain-boundary density, suggesting a higher grain-boundary density in the experimental system. Alternatively, the atomistic grain boundary structure could be different between experiment and simulation: experimentally there may be residual amorphous phases or a higher degree of structural disorder between crystalline grains. The results raise the question of the origin of the ionically blocking behavior at the grain boundaries. The low activation energy observed for electronic transport might suggest that a high space charge barrier is not present and might indicate rather a lowering of oxide ion mobility at boundaries due to, e.g., disruption of atomic periodicity. From MD simulations, however, it is not possible to extract the charge densities, owing to the small perturbations from the charge-neutral state and the boundaries not being planar. We are therefore unable to rule out either space charge or structural factors.

One may also consider the possible relationship of lattice strain/distortions to ionic conductivity in this work. An increase in unit cell volume and structural distortions (i.e., deviation from cubic symmetry) in $La_{1-x}Sr_xFe_{1-y}Ga_yO_{3-x}$ upon Ga substitution has been associated with higher ionic conductivity (for

temperatures below 900 °C) and lower activation energy for ionic transport,[31] albeit at the expense of the p-type conductivity. A combined experimental and computational study on the impact of structural parameters on ionic conductivity in epitaxial $La_{0.9}Sr_{0.1}Ga_{0.95}Mg_{0.05}O_{3-d}$ thin films found that increasing unit cell volume lowers migration barriers while large octahedral rotations create low-energy migration pathways.[20] In the present work, an initial increase and subsequent decrease in unit cell volume in the crystalline regions is observed via in situ GIXRD during crystallization (Figure 3e,f) (along with convergence of the pseudocubic lattice parameters); however, the simultaneously measured ionic conductivity does not follow the same trend after the onset of crystallization (Figure 5). Unlike the epitaxial thin films in the aforementioned study on LSGM, the crystallized LSGF films are polycrystalline with a large volume fraction of grain boundaries and possible residual amorphous regions (Figure 4). This microstructural difference suggests that the processing route and resultant microstructure may dominate the ionic charge transport behavior compared to crystal structure and/or strain effects. Hypothetically, if the grain, grain boundary, and amorphous ionic conductivity responses were separable one might see the grain ionic conductivity follow the lattice parameter evolution.

4.4. Electronic Conductivity, Total Conductivity, and Transference Number Evolution

Along with the increase in ionic conductivity, the total conductivity of amorphous-grown LSGF thin films increases rapidly during crystallization (Figure 6a), with the difference indicating an even more significant increase in electronic conductivity. We tentatively attribute this change in electronic conductivity to an increase in both hole concentration (more dominant) and mobility (less dominant). Under oxidizing conditions, holes are the majority electronic charge carriers in crystalline LSGF, with hole concentration increasing as oxygen content increases for charge neutrality. In STF35 thin films under the same conditions, oxidation was directly observed to occur with the onset of crystallization,[17] and the comparable color change as a result of crystallization observed for LSGF in this work suggests a consistent oxidation process that increases the hole concentration. Electronic conduction in LSGF proceeds through the directional O 2p and Fe 3d orbitals in a polaron hopping mechanism.[59] We expect the hole mobility to depend on the O 2p – Fe 3d orbital overlap, which in turn is likely related to the symmetry and alignment of neighboring Fe coordination units. In a perfectly cubic structure, maximum orbital overlap is achieved. Deviations from cubic structures are expected to result in a decrease in hole mobility,[17,31] although bond lengths may play a role too. In the related STF35 system, the B-site cation coordination units become more symmetric and better aligned with their neighbors with the onset of oxidation and crystallization, reducing the structural disorder in the system.[17] In the present work, the convergence of pseudocubic lattice parameters as crystallization progresses suggests an ongoing similar structural trend toward increased alignment of B-site coordination units even after the onset of crystallization. Therefore, a similar combination of increase in hole concentration from oxidation and hole mobility from increasing symmetry could reasonably explain the observed dramatic increase in total conductivity in the LSGF composition used in this work.

A comparison of temperature-dependent AC-IS measurements with and without blocking electrodes before and after crystallization shows that the electronic conductivity increases much more significantly than the ionic conductivity, such that the material transitions from a predominantly ionic conductor to a predominantly electronic conductor with increasing crystallinity. The ionic transference number (Figure 6c) calculated from the temperature-dependent AC-IS measurements decreases during crystallization from nearly 1 as-deposited to nearly 0 after crystallization. The low activation energy of 0.35 eV for total conductivity after crystallization (Figure 6a) is consistent with reports[29,51] indicating a dominant (p-type) electronic contribution.[29,60] A recent DFT study shows that electronic conduction in $La_{1-x}Sr_xFeO_{3-d}$ (LSF) arises from a hole polaron hopping mechanism, with the self-trapped holes shared between hybridized Fe 3d and O 2p orbitals, yielding a mobility activation energy ranging from 0.3 to 0.4 eV.[59] Given the similar measured activation energy for total conductivity in the present work, a polaron mechanism is reasonable and may suggest very little contribution to the activation energy from thermally-activated electronic carrier generation under these conditions. DC polarization studies on amorphous LSGF and in situ crystallized LSGF (Figure 8) confirm the decrease in ionic transference number with increasing crystallinity.

Not just the magnitude, but the rate by which the total versus ionic conductivities increase also appears to differ, with electronic conductivity increasing more rapidly during isothermal crystallization (Figure 5). As discussed above, the changes in electronic and ionic conductivity proceed by different mechanisms. We suggest that the electronic conductivity is highly dependent on oxidation (suggested by the color change) and to a lesser extent on the alignment of Fe-O polyhedra, which occur rapidly with crystallization (according to prior work on the related STF35 composition).[17] The ionic conductivity may depend in a more complex way on the local structural order and strain that influence the energy landscape within the grains but also significantly on the ionically blocking grain-boundary density. On top of these differences, oxidation increases the electronic carrier (hole) concentration but presumably decreases the ionic carrier (oxygen vacancy) concentration or oxygen deficiency (since vacancies cannot be defined in the amorphous structure, at least not in the same way as for a crystalline phase). The role of increased surface area-to-volume ratio arising from pore formation on the ionic and electronic transport is not yet known, but we note that the internal surfaces may not be fully interconnected/percolating. The appearance of porosity likely suppresses both ionic and electronic conductances, as suggested by an effective medium approach to composite behavior.

It remains to be seen whether the evolution of transport behavior and structure observed in this work is unique to PLD-grown amorphous films or generalizable across different synthesis routes. Because the initial oxygen deficiency of amorphous PLD films is hypothesized to control the evolution of defect chemistry and microstructure as films crystallize and simultaneously oxidize, the behavior might be replicated via other low-temperature film routes, if those can also yield the

low-electron-density, under-coordinated structures expected of amorphous phases.

5. Summary and Conclusion

After room-temperature pulsed laser deposition of amorphous LSGF thin films, we investigated the effect of crystallization on the dynamic evolution of ionic and electronic transport behavior. Temperature-dependent total conductivity and ionic conductivity measurements were conducted during crystallization using A.C. impedance spectroscopy (AC-IS) with reversible or electronically blocking electrodes, enabling estimation of ionic transference numbers before, during, and after crystallization at various temperatures as well as ionic versus total conductivity activation energies. Isothermal ionic transference numbers were also evaluated at various stages of crystallization using a DC polarization technique. Additional isothermal in situ synchrotron GIXRD with simultaneous AC-IS measurements (with blocking and reversible electrodes) during crystallization were conducted to directly correlate the evolving crystal structure to the total and ionic conductivity. The related changes in the microstructure of as-deposited versus crystallized (after 20 min and 3 h at 700 °C) films were imaged using bright-field TEM and HAADF STEM to understand the contributions of grain boundaries and porosity. Finally, given the observation of a high grain-boundary density and high ionic conductivity activation energy after crystallization, MD simulations were performed to assess oxygen tracer diffusivity and activation enthalpy as a function of grain boundary density.

From these results, we observed that amorphous LSGF thin films crystallize directly into an orthorhombic perovskite structure with no evidence of secondary phase formation. The crystallinity of the films increases with time when annealed at 700 °C, as evidenced by the decrease in intensity of the amorphous hump and the appearance of diffraction peaks from in situ GIXRD. The structure of the crystalline regions ultimately approaches a cubic structure during ongoing crystallization, with complex lattice strain evolution (expansion then contraction). From S/TEM imaging, extensive porosity forms during crystallization, with the connectivity of pore chains increasing with crystallinity, and a high grain boundary density is present after grain nucleation with grain diameters on the order of ≈10 s of nm. Although the ionic conductivity increases by ≈2 orders of magnitude during crystallization, the electronic conductivity increases even more significantly, such that the material transitions from being a predominantly ionic conductor to a predominantly electronic conductor as crystallinity increases. The relatively low ionic conductivity compared to bulk LSGF reported in the literature and an observed increase in activation energy for ionic conduction after crystallization in this study suggests that ionically blocking grain boundaries heavily influence ionic transport in crystallized (nanocrystalline) LSGF. Molecular dynamics simulations also show an increase in oxide-ion migration enthalpy with increasing grain boundary density, providing further support for this interpretation. Altogether, the GIXRD, electrical, MD, and microscopy analyses suggest that the oxide-ion transport behavior is significantly influenced by the evolution of both local atomic structural order and microstructure, while the electronic conductivity is influenced by the former along with the change in hole concentration attributed to oxidation during crystallization. Grain boundaries appear to be relatively nonblocking to electronic carriers (compared to oxide ions) in this composition, considering the low activation energy for total (electronic-dominated) conductivity in the nanocrystalline films. By tuning both the crystallinity and microstructure, the ionic transference number can be tailored widely, to access ionic-dominant, mixed, and electronic-dominant conducting regimes – without altering the cation composition. These results show further promise for the use of low-temperature-processed, semi-crystalline mixed conductors across a broad range of low-to-intermediate temperature solid-state-ionic applications.

Supporting Information

Supporting Information is available from the Wiley Online Library or from the author.

Acknowledgements

The authors gratefully acknowledge primary funding for this work from the U.S. Department of Energy, Basic Energy Sciences, Materials Chemistry program under grant number DE-SC-0018963 (to NHP). Authors acknowledge the use of shared equipment in the Illinois Materials Research Laboratory at the University of Illinois Urbana-Champaign, including the Bruker D8 XRD equipment supported by NSF through the University of Illinois at Urbana-Champaign Materials Research Science and Engineering Center DMR-2309037. Emily Skiba is acknowledged for assistance with the collection of simultaneous GIXRD/AC-IS data at APS beamline 12-ID-D. This research used resources of the Advanced Photon Source, a U.S. Department of Energy (DOE) Office of Science user facility operated for the DOE Office of Science by Argonne National Laboratory under Contract No. DE-AC02-06CH11357.

Conflict of Interest

The authors declare no conflict of interest.

Author Contributions

HBB - Methodology, Validation, Formal Analysis, Investigation, Data Curation, Writing – Original Draft, Visualization; JSG – Formal Analysis, Investigation; AB – Formal Analysis, Investigation, Data Curation, Writing – Original Draft, Visualization; KR - Investigation, HZ - Resources, Data Curation, Writing – Review & Editing; RAD – Methodology, Software, Resources, Writing – Review & Editing, Supervision (AB, KR); NHP – Conceptualization, Methodology, Validation, Formal Analysis, Resources, Writing – Review & Editing, Visualization, Supervision (HBB, JSG), Project Administration, Funding Acquisition.

Data Availability Statement

The data that support the findings of this study are available from the corresponding author upon reasonable request.

Keywords

crystallization, grain boundary, mixed ionic/electronic conductor, oxide-ion transport, polaron

Received: January 30, 2024
Revised: June 4, 2024
Published online: June 29, 2024

[1] T. T. Mayeshiba, D. D. Morgan, *Solid State Ion* **2016**, *296*, 71.
[2] S. B. Adler, *Chem. Rev.* **2004**, *104*, 4791.
[3] D. J. L. Brett, A. Atkinson, N. P. Brandon, S. J. Skinner, *Chem. Soc. Rev.* **2008**, *37*, 1568.
[4] W. Jung, H. L. Tuller, *ECS Trans.* **2019**, *35*, 2129.
[5] W. Jung, H. L. Tuller, *J. Electrochem. Soc.* **2008**, *155*, B1194.
[6] S. R. Bishop, T. S. Stefanik, H. L. Tuller, *Phys. Chem. Chem. Phys.* **2011**, *13*, 10165.
[7] N. H. Perry, D. Pergolesi, S. R. Bishop, H. L. Tuller, *Solid State Ion* **2015**, *273*, 18.
[8] Y. Chen, W. Jung, Z. Cai, J. J. Kim, H. L. Tuller, B. Yildiz, *Energy Environ. Sci.* **2012**, 7979.
[9] B. Koo, K. Kim, J. K. Kim, H. Kwon, J. W. Han, W. C. Jung, *Joule* **2018**, *2*.
[10] S. R. Bishop, D. Marrocchelli, C. Chatzichristodoulou, N. H. Perry, M. B. Mogensen, H. L. Tuller, E. D. Wachsman, *Annu. Rev. Mater. Res.* **2014**, *44*, 205.
[11] D. Marrocchelli, N. H. Perry, S. R. Bishop, *Phys. Chem. Chem. Phys.* **2015**, *17*, 10028.
[12] N. H. Perry, J. J. Kim, S. R. Bishop, H. L. Tuller, *J. Mater. Chem. A* **2015**, *3*, 3602.
[13] K. Sato, T. Hashida, K. Yashiro, H. Yugami, T. Kawada, J. Mizusaki, *J. Ceram. Soc. Jpn.* **2005**, *113*, 562.
[14] A. Cavallaro, S. S. Pramana, E. Ruiz-Trejo, P. C. Sherrell, E. Ware, J. A. Kilner, S. J. Skinner, *Sustain Energy Fuels* **2018**, *2*, 862.
[15] A. Evans, J. Martynczuk, D. Stender, C. W. Schneider, T. Lippert, M. Prestat, *Adv. Energy Mater.* **2015**, *5*, 1400747.
[16] J. Januschewsky, M. Ahrens, A. Opitz, F. Kubel, J. Fleig, *Adv. Funct. Mater.* **2009**, *19*, 3151.
[17] H. B. Buckner, Q. Ma, J. Simpson-Gomez, E. J. Skiba, N. H. Perry, *J. Mater. Chem. A* **2021**, 2421.
[18] T. Chen, G. F. Harrington, K. Sasaki, N. H. Perry, *J. Mater. Chem. A* **2017**, *5*, 23006.
[19] T. Chen, G. F. Harrington, J. Masood, K. Sasaki, N. H. Perry, *ACS Appl. Mater. Interfaces* **2019**, *11*, 9102.
[20] M. Cherry, M. S. Islam, C. R. A. Catlow, *J. Solid State Chem.* **1995**, *118*.
[21] R. Gao, A. C. P. Jain, S. Pandya, Y. Dong, Y. Yuan, H. Zhou, L. R. Dedon, V. Thoréton, S. Saremi, R. Xu, A. Luo, T. Chen, V. Gopalan, E. Ertekin, J. Kilner, T. Ishihara, N. H. Perry, D. R. Trinkle, L. W. Martin, *Adv. Mater.* **2020**, *32*, 1905178.
[22] T. Ishihara, J. A. Kilner, M. Honda, Y. Takita, *J. Am. Chem. Soc.* **1997**, *119*, 2747.
[23] K. Huang, R. S. Tichy, J. B. Goodenough, *J. Am. Ceram. Soc.* **1998**, *81*, 2587.
[24] K. Huang, M. Feng, J. B. Goodenough, C. Milliken, *J. Electrochem. Soc.* **1997**, *144*, 3627.
[25] M. Enoki, J. Yan, H. Matsumoto, T. Ishihara, *Solid State Ion* **2006**, *177*, 2053.
[26] T. Ishigaki, S. Yamauchi, K. Kishio, J. Mizusaki, K. Fueki, *J. Solid State Chem.* **1988**, *73*, 179.
[27] Y. Tsuruta, T. Todaka, H. Nisiguchi, T. Ishihara, Y. Takita, *Electrochem. Solid-State Lett.* **2001**, *4*, E13.
[28] T. Ishihara, T. Yamada, H. Arikawa, H. Nishiguchi, Y. Takita, *Solid State Ion* **2000**, *135*, 631.
[29] V. V. Kharton, A. P. Viskup, A. A. Yaremchenko, R. T. Baker, B. Gharbage, G. C. Mather, F. M. Figueiredo, E. N. Naumovich, F. M. B. Marques, *Solid State Ion* **2000**, *132*, 119.
[30] D. P. Fagg, V. V. Kharton, J. R. Frade, a a L. Ferreira, *Solid State Ion* **2003**, *156*, 45.
[31] V. V. Kharton, A. L. Shaulo, A. P. Viskup, M. Avdeev, A. A. Yaremchenko, M. V. Patrakeev, A. I. Kurbakov, E. N. Naumovich, F. M. B. Marques, *Solid State Ion* **2002**, *150*, 229.
[32] N. P. Vyshatko, V. Kharton, A. L. Shaula, E. N. Naumovich, F. M. B. Marques, *Mater. Res. Bull.* **2003**, *38*, 185.
[33] V. Thoréton, M. Niania, J. Druce, H. Tellez, J. A. Kilner, *J. Electrochem. Soc.* **2022**, *169*, 044513.
[34] A. Bonkowski, J. A. Kilner, R. A. De Souza, *RSC Appl. Interfaces* **2024**, https://pubs.rsc.org/en/content/articlelanding/2024/lf/d3lf00263b.
[35] V. Metlenko, A. H. H. Ramadan, F. Gunkel, H. Du, H. Schraknepper, S. Hoffmann-Eifert, R. Dittmann, R. Waser, R. A. De Souza, *Nanoscale* **2014**, *6*, 12864.
[36] R. A. De Souza, *J. Mater. Chem. A Mater.* **2017**, *5*, 20334.
[37] T. H. Wan, M. Saccoccio, C. Chen, F. Ciucci, *Electrochim. Acta.* **2015**, *184*, 483.
[38] W. Tang, G. Chang, H. Yuan, L. Zhao, Z. Liu, P. Ming, X. Wei, H. Dai, *Energy Convers Manag.* **2022**, *272*.
[39] F. Kullmann, M. Mueller, A. Lindner, S. Dierickx, E. Mueller, A. Weber, *J. Power Sources* **2023**, *587*, 233706.
[40] J. Uecker, I. D. Unachukwu, V. Vibhu, I. C. Vinke, R. A. Eichel, L. G. J. (Bert) de Haart, *Electrochim. Acta.* **2023**, *452*, 142320.
[41] I. D. Unachukwu, V. Vibhu, I. C. Vinke, R. A. Eichel, L. G. J. (Bert) de Haart, *J. Power Sources* **2023**, *556*.
[42] C. Peters, A. Weber, B. Butz, D. Gerthsen, E. Ivers-Tiffée, *J. Am. Ceram. Soc.* **2009**, *92*, 2017.
[43] M. Gerstl, E. Navickas, G. Friedbacher, F. Kubel, M. Ahrens, J. Fleig, *Solid State Ion* **2011**, *185*, 32.
[44] J. H. Joo, G. M. Choi, *Solid State Ion* **2006**, *177*.
[45] S. Heiroth, T. Lippert, A. Wokaun, M. Döbeli, *Appl. Phys. A Mater. Sci. Process* **2008**, *93*, 639.
[46] A. P. Thompson, H. M. Aktulga, R. Berger, D. S. Bolintineanu, W. M. Brown, P. S. Crozier, P. J. in 't Veld, A. Kohlmeyer, S. G. Moore, T. D. Nguyen, R. Shan, M. J. Stevens, J. Tranchida, C. Trott, S. J. Plimpton, *Comput. Phys. Commun.* **2022**, *271*, 108171.
[47] M. S. Islam, M. Cherry, C. R. A. Catlow, *J. Solid State Chem.* **1996**, *124*, 230.
[48] M. S. Khan, M. S. Islam, D. R. Bates, *J. Phys. Chem. B.* **1998**, *102*, 3099.
[49] P. Hirel, *Comput. Phys. Commun.* **2015**, *197*, 212.
[50] E. Juste, A. Julian, G. Etchegoyen, P. M. Geffroy, T. Chartier, N. Richet, P. Del Gallo, *J Memb Sci.* **2008**, *319*, 185.
[51] S. Koutcheiko, P. Whitfield, I. Davidson, *Ceram. Int.* **2006**, *32*, 339.
[52] G. C. Kostogloudis, C. Ftikos, A. Ahmad-Khanlou, A. Naoumidis, D. Stöver, *Solid State Ion.* **2000**, *134*, 127.
[53] K. Huang, R. S. Tichy, J. B. Goodenough, *J. Am. Ceram. Soc.* **1998**, *81*, 2565.
[54] N. M. Sammes, G. A. Tompsett, R. J. Phillips, A. M. Cartner, *Solid State Ion* **1998**, *111*, 1.
[55] D. Ehre, H. Cohen, V. Lyahovitskaya, A. Tagantsev, I. Lubomirsky, *Adv. Funct. Mater.* **2007**, *17*, 1204.
[56] T. Ishihara, Y. Tsuruta, Y. Chunying, T. Todaka, H. Nishiguchi, Y. Takita, *J. Electrochem. Soc.* **2003**, *150*, E17.
[57] V. V. Kharton, A. A. Yaremchenko, A. P. Viskup, M. V. Patrakeev, I. A. Leonidov, V. L. Kozhevnikov, F. M. Figueiredo, A. L. Shaulo, E. N. Naumovich, F. M. B. Marques, *J. Electrochem. Soc.* **2002**, *149*, E125.
[58] T. Chen, G. F. Harrington, J. Matsuda, K. Sasaki, D. Pham, E. L. Corral, N. H. Perry, *J. Electrochem. Soc.* **2019**, *166*, F569.
[59] C. Hartmann, J. Laurencin, G. Geneste, *Phys. Rev. B.* **2023**, *107*, 024104.
[60] S. Komine, E. Iguchi, *J. Phys. Chem. Solids* **2007**, *68*, 1504.